

Measurement of leading proton and neutron production in deep-inelastic scattering at HERA

H1 Collaboration

C. Adloff³⁴, M. Anderson²², V. Andreev²⁵, B. Andrieu²⁸, V. Arkadov³⁵, C. Arndt¹¹, I. Ayyaz²⁹, A. Babaev²⁴, J. Bähr³⁵, P. Baranov²⁵, E. Barrelet²⁹, W. Bartel¹¹, U. Bassler²⁹, P. Bate²², M. Beck¹³, A. Beglarian^{11,40}, O. Behnke¹¹, H.-J. Behrend¹¹, C. Beier¹⁵, A. Belousov²⁵, Ch. Berger¹, G. Bernardi²⁹, T. Berndt¹⁵, G. Bertrand-Coremans⁴, P. Biddulph²², J.C. Bizot²⁷, V. Boudry²⁸, W. Braunschweig¹, V. Brisson²⁷, D.P. Brown²², W. Brückner¹³, P. Bruel²⁸, D. Bruncko¹⁷, J. Bürger¹¹, F.W. Büsler¹², A. Buniatian³², S. Burke¹⁸, G. Buschhorn²⁶, D. Calvet²³, A.J. Campbell¹¹, T. Carli²⁶, E. Chabert²³, M. Charlet⁴, D. Clarke⁵, B. Clerbaux⁴, S. Cocks¹⁹, J.G. Contreras^{8,43}, C. Cormack¹⁹, J.A. Coughlan⁵, M.-C. Cousinou²³, B.E. Cox²², G. Cozzika¹⁰, J. Cvach³⁰, J.B. Dainton¹⁹, W.D. Dau¹⁶, K. Daum³⁹, M. David¹⁰, M. Davidsson²¹, A. De Roeck¹¹, E.A. De Wolf⁴, B. Delcourt²⁷, R. Demirchyan^{11,40}, C. Diaconu²³, M. Dirkmann⁸, P. Dixon²⁰, W. Dlugosz⁷, K.T. Donovan²⁰, J.D. Dowell³, A. Drouskoi²⁴, J. Ebert³⁴, G. Eckerlin¹¹, D. Eckstein³⁵, V. Efremenko²⁴, S. Egli³⁷, R. Eichler³⁶, F. Eisele¹⁴, E. Eisenhandler²⁰, E. Elsen¹¹, M. Enzenberger²⁶, M. Erdmann^{14,42.f}, A.B. Fahr¹², L. Favart⁴, A. Fedotov²⁴, R. Felst¹¹, J. Feltesse¹⁰, J. Ferencei¹⁷, F. Ferrarotto³², M. Fleischer⁸, G. Flügge², A. Fomenko²⁵, J. Formánek³¹, J.M. Foster²², G. Franke¹¹, E. Gabathuler¹⁹, K. Gabathuler³³, F. Gaede²⁶, J. Garvey³, J. Gassner³³, J. Gayler¹¹, R. Gerhards¹¹, S. Ghazaryan^{11,40}, A. Glazov³⁵, L. Goerlich⁶, N. Gogitidze²⁵, M. Goldberg²⁹, I. Gorelov²⁴, C. Grab³⁶, H. Grässler², T. Greenshaw¹⁹, R.K. Griffiths²⁰, G. Grindhammer²⁶, T. Hadig¹, D. Haidt¹¹, L. Hajduk⁶, T. Haller¹³, M. Hampel¹, V. Hausteim³⁴, W.J. Haynes⁵, B. Heinemann¹¹, G. Heinzelmann¹², R.C.W. Henderson¹⁸, S. Hengstmann³⁷, H. Henschel³⁵, R. Heremans⁴, I. Herynek³⁰, K. Hewitt³, K.H. Hiller³⁵, C.D. Hilton²², J. Hladký³⁰, D. Hoffmann¹¹, T. Holtom¹⁹, R. Horisberger³³, S. Hurling¹¹, M. Ibbotson²², Ç. İşsever⁸, M. Jacquet²⁷, M. Jaffre²⁷, D.M. Jansen¹³, L. Jönsson²¹, D.P. Johnson⁴, H. Jung²¹, H.K. Kästli³⁶, M. Kander¹¹, D. Kant²⁰, M. Kapichine⁹, M. Karlsson²¹, O. Karschnik¹², J. Katzy¹¹, O. Kaufmann¹⁴, M. Kausch¹¹, I.R. Kenyon³, S. Kermiche²³, C. Keuker¹, C. Kiesling²⁶, M. Klein³⁵, C. Kleinwort¹¹, G. Knies¹¹, J.H. Köhne²⁶, H. Kolanoski³⁸, S.D. Kolya²², V. Korbel¹¹, P. Kostka³⁵, S.K. Kotelnikov²⁵, T. Krämerkampfer⁸, M.W. Krasny²⁹, H. Krehbiel¹¹, D. Krücker²⁶, K. Krüger¹¹, A. Küpper³⁴, H. Küster², M. Kühlen²⁶, T. Kurča³⁵, R. Lahmann¹¹, M.P.J. Landon²⁰, W. Lange³⁵, U. Langenegger³⁶, A. Lebedev²⁵, F. Lehner¹¹, V. Lemaître¹¹, V. Lendermann⁸, S. Levonian¹¹, M. Lindstroem²¹, B. List¹¹, G. Lobo²⁷, E. Lobodzinska^{6,41}, V. Lubimov²⁴, S. Lüders³⁶, D. Lüke^{8,11}, L. Lytkin¹³, N. Magnussen³⁴, H. Mahlke-Krüger¹¹, E. Malinowski²⁵, R. Maraček¹⁷, P. Marage⁴, J. Marks¹⁴, R. Marshall²², G. Martin¹², H.-U. Martyn¹, J. Martyniak⁶, S.J. Maxfield¹⁹, S.J. McMahon¹⁹, T.R. McMahon¹⁹, A. Mehta⁵, K. Meier¹⁵, P. Merkel¹¹, F. Metlica¹³, A. Meyer¹¹, A. Meyer¹¹, H. Meyer³⁴, J. Meyer¹¹, P.-O. Meyer², S. Mikocki⁶, D. Milstead¹¹, J. Moeck²⁶, R. Mohr²⁶, S. Mohrdieck¹², F. Moreau²⁸, J.V. Morris⁵, D. Müller³⁷, K. Müller¹¹, P. Murín¹⁷, V. Nagovizin²⁴, B. Naroska¹², Th. Naumann³⁵, I. Négre²³, P.R. Newman³, H.K. Nguyen²⁹, T.C. Nicholls¹¹, F. Niebergall¹², C. Niebuhr¹¹, Ch. Niedzballa¹, H. Niggli³⁶, D. Nikitin⁹, O. Nix¹⁵, G. Nowak⁶, T. Nunnemann¹³, H. Oberlack²⁶, J.E. Olsson¹¹, D. Ozerov²⁴, P. Palmen², V. Panassik⁹, C. Pascaud²⁷, S. Passaggio³⁶, G.D. Patel¹⁹, H. Pawletta², E. Perez¹⁰, J.P. Phillips¹⁹, A. Pieuchot¹¹, D. Pitzl³⁶, R. Pöschl⁸, G. Pope⁷, B. Povh¹³, K. Rabbertz¹, J. Rauschenberger¹², P. Reimer³⁰, B. Reisert²⁶, H. Rick¹¹, S. Riess¹², E. Rizvi¹¹, P. Robmann³⁷, R. Roosen⁴, K. Rosenbauer¹, A. Rostovtsev^{24,12}, F. Rouse⁷, C. Royon¹⁰, S. Rusakov²⁵, K. Rybicki⁶, D.P.C. Sankey⁵, P. Schacht²⁶, J. Scheins¹, F.-P. Schilling¹⁴, S. Schleif¹⁵, P. Schleper¹⁴, D. Schmidt³⁴, D. Schmidt¹¹, L. Schoeffel¹⁰, V. Schröder¹¹, H.-C. Schultz-Coulon¹¹, B. Schwab¹⁴, F. Sefkow³⁷, A. Semenov²⁴, V. Shekelyan²⁶, I. Sheviakov²⁵, L.N. Shtarkov²⁵, G. Siegmon¹⁶, Y. Sirois²⁸, T. Sloan¹⁸, P. Smirnov²⁵, M. Smith¹⁹, V. Solochenko²⁴, Y. Soloviev²⁵, V. Spaskov⁹, A. Specka²⁸, J. Spiekermann⁸, H. Spitzer¹², F. Squinabol²⁷, P. Steffen¹¹, R. Steinberg², J. Steinhart¹², B. Stella³², A. Stellberger¹⁵, J. Stiewe¹⁵, U. Straumann¹⁴, W. Struczinski², J.P. Sutton³, M. Swart²⁰, S. Tapprogge¹⁵, M. Taševský³⁰, V. Tchernyshov²⁴, S. Tchetchelnitski²⁴, J. Theissen², G. Thompson²⁰, P.D. Thompson³, N. Tobien¹¹, R. Todenhagen¹³, P. Truöl³⁷, G. Tsipolitis³⁶, J. Turnau⁶, E. Tzamariudaki¹¹, S. Udluft²⁶, A. Usik²⁵, S. Valkár³¹, A. Valkárová³¹, C. Vallée²³, P. Van Esch⁴, A. Van Haecke¹⁰, P. Van Mechelen⁴, Y. Vazdik²⁵, G. Villet¹⁰, K. Wacker⁸, R. Wallny¹⁴, T. Walter³⁷, B. Waugh²², G. Weber¹², M. Weber¹⁵, D. Wegener⁸, A. Wegner²⁶, T. Wengler¹⁴, M. Werner¹⁴, L.R. West³, S. Wiesand³⁴, T. Wilksen¹¹, S. Willard⁷, M. Winde³⁵, G.-G. Winter¹¹, C. Wittek¹², E. Wittmann¹³, M. Wobisch², H. Wollatz¹¹, E. Wünsch¹¹, J. Žáček³¹, J. Zálešák³¹, Z. Zhang²⁷, A. Zhokin²⁴, P. Zini²⁹, F. Zomer²⁷, J. Zsembery¹⁰, M. zurNedden³⁷

- ¹ I. Physikalisches Institut der RWTH, Aachen, Germany^a
² III. Physikalisches Institut der RWTH, Aachen, Germany^a
³ School of Physics and Space Research, University of Birmingham, Birmingham, UK^b
⁴ Inter-University Institute for High Energies ULB-VUB, Brussels; Universitaire Instelling Antwerpen, Wilrijk; Belgium^c
⁵ Rutherford Appleton Laboratory, Chilton, Didcot, UK^b
⁶ Institute for Nuclear Physics, Cracow, Poland^d
⁷ Physics Department and IIRPA, University of California, Davis, CA, USA^e
⁸ Institut für Physik, Universität Dortmund, Dortmund, Germany^a
⁹ Joint Institute for Nuclear Research, Dubna, Russia
¹⁰ DSM/DAPNIA, CEA/Saclay, Gif-sur-Yvette, France
¹¹ DESY, Hamburg, Germany^a
¹² II. Institut für Experimentalphysik, Universität Hamburg, Hamburg, Germany^a
¹³ Max-Planck-Institut für Kernphysik, Heidelberg, Germany^a
¹⁴ Physikalisches Institut, Universität Heidelberg, Heidelberg, Germany^a
¹⁵ Institut für Hochenergiephysik, Universität Heidelberg, Heidelberg, Germany^a
¹⁶ Institut für experimentelle und angewandte Physik, Universität Kiel, Kiel, Germany^a
¹⁷ Institute of Experimental Physics, Slovak Academy of Sciences, Košice, Slovak Republic^{f,j}
¹⁸ School of Physics and Chemistry, University of Lancaster, Lancaster, UK^b
¹⁹ Department of Physics, University of Liverpool, Liverpool, UK^b
²⁰ Queen Mary and Westfield College, London, UK^b
²¹ Physics Department, University of Lund, Lund, Sweden^g
²² Department of Physics and Astronomy, University of Manchester, Manchester, UK^b
²³ CPPM, Université d'Aix-Marseille II, IN2P3-CNRS, Marseille, France
²⁴ Institute for Theoretical and Experimental Physics, Moscow, Russia
²⁵ Lebedev Physical Institute, Moscow, Russia^{f,k}
²⁶ Max-Planck-Institut für Physik, München, Germany^a
²⁷ LAL, Université de Paris-Sud, IN2P3-CNRS, Orsay, France
²⁸ LPNHE, École Polytechnique, IN2P3-CNRS, Palaiseau, France
²⁹ LPNHE, Universités Paris VI and VII, IN2P3-CNRS, Paris, France
³⁰ Institute of Physics, Academy of Sciences of the Czech Republic, Praha, Czech Republic^{f,h}
³¹ Nuclear Center, Charles University, Praha, Czech Republic^{f,h}
³² INFN Roma 1 and Dipartimento di Fisica, Università Roma 3, Roma, Italy
³³ Paul Scherrer Institut, Villigen, Switzerland
³⁴ Fachbereich Physik, Bergische Universität Gesamthochschule Wuppertal, Wuppertal, Germany^a
³⁵ DESY, Institut für Hochenergiephysik, Zeuthen, Germany^a
³⁶ Institut für Teilchenphysik, ETH, Zürich, Switzerlandⁱ
³⁷ Physik-Institut der Universität Zürich, Zürich, Switzerlandⁱ
³⁸ Institut für Physik, Humboldt-Universität, Berlin, Germany^a
³⁹ Rechenzentrum, Bergische Universität Gesamthochschule Wuppertal, Wuppertal, Germany^a
⁴⁰ Visitor from Yerevan Physics Institute, Armenia
⁴¹ Foundation for Polish Science fellow
⁴² Institut für Experimentelle Kernphysik, Universität Karlsruhe, Karlsruhe, Germany
⁴³ Dept. Fís. Ap. CINVESTAV, Mérida, Yucatán, México

Received: 7 November 1998 / Published online: 25 January 1999

Abstract. Deep-inelastic scattering events with a leading baryon have been detected by the H1 experiment at HERA using a forward proton spectrometer and a forward neutron calorimeter. Semi-inclusive cross sections have been measured in the kinematic region $2 \leq Q^2 \leq 50 \text{ GeV}^2$, $6 \times 10^{-5} \leq x \leq 6 \times 10^{-3}$ and baryon $p_T \leq 200 \text{ MeV}$, for events with a final-state proton with energy $580 \leq E' \leq 740 \text{ GeV}$, or a neutron with energy $E' \geq 160 \text{ GeV}$. The measurements are used to test production models and factorization hypotheses. A Regge model of leading baryon production which consists of pion, pomeron and secondary reggeon exchanges gives an acceptable description of both semi-inclusive cross sections in the region $0.7 \leq E'/E_p \leq 0.9$, where E_p is the proton beam energy. The leading neutron data are used to estimate for the first time the structure function of the pion at small Bjorken- x .

^a Supported by the Bundesministerium für Bildung, Wissenschaft, Forschung und Technologie, FRG, under contract numbers 7AC17P, 7AC47P, 7DO55P, 7HH17I, 7HH27P, 7HD17P, 7HD27P, 7KI17I, 6MP17I and 7WT87P

^b Supported by the UK Particle Physics and Astronomy Research Council, and formerly by the UK Science and Engineering Research Council

^c Supported by FNRS-FWO, IISN-IKW

1 Introduction

We report the measurement of the semi-inclusive cross sections for proton and neutron production in deep-inelastic scattering (DIS). The $ep \rightarrow eNX$ data, where N represents either a final-state proton or neutron, were obtained during 1995 and 1996 using the HERA accelerator at DESY where 27.5 GeV positrons collided with 820 GeV protons. Events containing leading baryons were detected using the H1 detector upgraded with a forward proton spectrometer (FPS) and a forward neutron calorimeter (FNC).

The two multi-purpose experiments at HERA, H1 and ZEUS, have observed a class of events which are characterized by the absence of final-state particles in the region of phase space between the outgoing proton debris and the current jet [1, 2]. These so-called rapidity gap events contribute approximately 10% to the total DIS cross section and can be interpreted as being mainly due to interactions of a virtual photon with a pomeron [3–6]. In addition to virtual photon-pomeron interactions, one also expects meson exchanges to contribute to the total DIS cross section and to the production of leading protons and neutrons with small p_T [7–10]. Due to its small mass the most obvious candidate for such an exchange is the pion. If only pion exchange is responsible for leading baryon production and if isospin is conserved at the proton vertex, the ratio of neutron and proton production should be equal to two due to the difference in the Clebsch–Gordan coefficients for the π^+n and π^0p isospin- $\frac{1}{2}$ states.

In this paper we present measurements of the semi-inclusive cross sections for proton and neutron production in the same kinematic region of x , Q^2 and p_T , where x is the Bjorken scaling variable, Q^2 is the negative four-momentum squared of the virtual photon and p_T is the transverse momentum of the final-state baryon with respect to the beam direction. The measurements are compared to the results of a Regge model of leading baryon production and are used to test the pion exchange expectation for the ratio of neutron and proton production. We also compare our measurements to the predictions of the LEPTO 6.5 Monte Carlo program [11] which simulates baryon production without Regge dynamics by using an alternative formalism based upon soft colour interactions [12, 13] and the string fragmentation model [14]. Our cross section measurements are relevant for the determination of fracture functions which are a perturbative QCD

approach for describing the semi-inclusive production of hadrons in the proton fragmentation region [15–17].

We use the kinematic variables x , Q^2 and y to describe the inclusive DIS process. They are defined as:

$$x = \frac{-q^2}{2p \cdot q} \quad Q^2 = -q^2 \quad y = \frac{p \cdot q}{p \cdot k}, \quad (1)$$

where p , k and q are the four-momenta of the incident proton, the incident positron and the exchanged vector boson (γ^*) coupling to the positron. At ep centre-of-mass energy \sqrt{s} they are related by $Q^2 = sxy$.

The kinematic variables used to describe a final-state baryon are:

$$t = (p - p')^2 \simeq -\frac{p_T^2}{z} - (1 - z) \left(\frac{m_N^2}{z} - m_p^2 \right) \\ z = 1 - \frac{q \cdot (p - p')}{q \cdot p} \simeq E'/E_p, \quad (2)$$

where p' is the four-momentum of the final-state baryon, m_N is the mass of the final-state baryon and m_p is the proton mass. As defined, t corresponds to the squared four-momentum transferred between the incident proton and the final-state baryon. It is different from the ‘rapidity gap’ definition $t = (p - p_Y)^2$ (used for example in [5]), which defines the hadronic system Y at the proton vertex by the presence of a rapidity gap. For leading baryon production the definition of t in this paper is more appropriate even though it is only equal to the rapidity gap definition for events where the final-state baryon is exclusively produced at the proton vertex.

The four-fold differential cross section for baryon production can be parameterized by a semi-inclusive structure function, $F_2^{\text{LB}(4)}$, defined by:

$$\frac{d^4\sigma(ep \rightarrow eNX)}{dx dQ^2 dz dt} = \frac{4\pi\alpha^2}{x Q^4} \left(1 - y + \frac{y^2}{2[1 + R(x, Q^2, z, t)]} \right) \\ \times F_2^{\text{LB}(4)}(x, Q^2, z, t), \quad (3)$$

where α is the fine structure constant and R is the ratio between the absorption cross sections for longitudinally and transversely polarized virtual photons. In the kinematic range covered by this analysis, the structure function $F_2^{\text{LB}(4)}$ is rather insensitive to the value of R and we assume that $R = 0$. The variation from $R = 0$ to $R = \infty$ leads to a 9% change at most in the resulting value of $F_2^{\text{LB}(4)}$ for the range of y covered in this measurement.

The four-fold differential cross section integrated over $0 \leq p_T \leq 200$ MeV defines the semi-inclusive structure function $F_2^{\text{LB}(3)}$ which we measure:

$$\frac{d^3\sigma(ep \rightarrow eNX)}{dx dQ^2 dz} = \int_{t_0}^{t_{\min}} \frac{4\pi\alpha^2}{x Q^4} \left(1 - y + \frac{y^2}{2} \right) \\ \times F_2^{\text{LB}(4)}(x, Q^2, z, t) dt \quad (4) \\ = \frac{4\pi\alpha^2}{x Q^4} \left(1 - y + \frac{y^2}{2} \right) F_2^{\text{LB}(3)}(x, Q^2, z),$$

^d Partially supported by the Polish State Committee for Scientific Research, grant no. 115/E-343/SPUB/P03/002/97 and grant no. 2P03B 055 13

^e Supported in part by US DOE grant DE F603 91ER40674

^f Supported by the Deutsche Forschungsgemeinschaft

^g Supported by the Swedish Natural Science Research Council

^h Supported by GA ĆR grant no. 202/96/0214, GA AV ĆR grant no. A1010821 and GA UK grant no. 177

ⁱ Supported by the Swiss National Science Foundation

^j Supported by VEGA SR grant no. 2/5167/98

^k Supported by Russian Foundation for Basic Research grant no. 96-02-00019

where the integration limits are:

$$t_{\min} = -(1-z) \left(\frac{m_{\text{N}}^2}{z} - m_{\text{p}}^2 \right)$$

$$t_0 = -\frac{(200 \text{ MeV})^2}{z} + t_{\min}. \quad (5)$$

The structure function $F_2^{\text{LB}(3)}$ is denoted by $F_2^{\text{LP}(3)}$ and $F_2^{\text{LN}(3)}$ for the semi-inclusive processes which have final-state protons and neutrons respectively. We present measurements of $F_2^{\text{LP}(3)}$ in the range $0.73 \leq z \leq 0.88$ and of $F_2^{\text{LN}(3)}$ for $0.3 \leq z \leq 0.9$. In this paper we do not discuss the very high z region ($z \gtrsim 0.95$) which is most relevant for pomeron exchange and which has been used to measure the diffractive structure function $F_2^{\text{D}(3)}$ [3–6].

2 H1 Apparatus

The central H1 detector is described in detail in [18–20]. Here only the forward proton spectrometer, the forward neutron calorimeter and the crucial parts of the central H1 detector used in this analysis are described. The coordinate system convention used by the H1 experiment defines the positive z -axis, or ‘forward’ direction, as being that of the outgoing proton beam. The positive x -axis points towards the centre of the HERA ring.

The components of the central H1 detector which are essential for this analysis are the backward electromagnetic calorimeter (SPACAL), the liquid argon calorimeter (LAr) and the central and forward tracking systems. The SPACAL calorimeter is used to determine the energy of the scattered positron whereas the hadronic final state is measured by the LAr calorimeter and the tracking systems. The SPACAL calorimeter has an electromagnetic energy resolution equal to $\sigma(E)/E = 7.1\%/\sqrt{E[\text{GeV}]} \oplus 1\%$ as measured in an electron beam [19] and an angular acceptance of $153^\circ < \theta < 177.5^\circ$. The LAr calorimeter has a hadronic energy resolution equal to $\sigma(E)/E \simeq 0.5/\sqrt{E}$ (E in GeV) as measured in a pion beam [21] and covers an angular range between 4° and 154° . Charged track momenta are measured using the central jet chamber (CJC), which consists of two concentric drift chambers covering an angular range between 15° and 165° , and by using the forward tracking system, which covers the angular range between 7° and 25° . A uniform field of 1.15 T is produced using a superconducting solenoid which surrounds both the LAr calorimeter and the central tracking system. Luminosity is measured by detecting photons, from the Bethe–Heitler process $ep \rightarrow ep\gamma$, in a crystal calorimeter situated at $z = -103$ m.

2.1 Detection of leading protons

The final-state proton data were collected during 1995 with the H1 forward proton spectrometer [22,23]. In order to measure momenta of protons with scattering angles

$\theta \lesssim 0.5$ mrad with respect to the beam, the HERA machine magnets adjacent to the interaction region are employed as spectrometer elements. Protons which have lost more than 10% of their energy in ep interactions appear after about 80 m at a distance of several millimetres from the nominal orbit so that they can be registered in detectors close to the circulating beam. The detector elements are mounted inside plunger vessels, so called Roman Pots, which are retracted during injection and are brought close to the beam after stable luminosity conditions are reached. The particles detected by the FPS are assumed to be protons. This is in agreement with Monte Carlo calculations which show that approximately 98% of the charged particles observed in the FPS are protons.

During 1995 H1 operated two FPS stations, located 81 and 90 m away from the interaction point, which approach the beam from above. Each station is equipped with four planes of hodoscopes constructed of 1 mm scintillating fibres which are oriented $\pm 45^\circ$ with respect to the y -axis. The scintillating fibre hodoscopes are 6 cm wide and 2.5 cm in height and are sandwiched between planes of trigger scintillators as sketched in Fig. 1. Each scintillating fibre hodoscope has 240 scintillating fibres arranged in five densely packed layers. Four of the scintillating fibres, belonging to a common layer but separated by 11 fibres from each other, are attached to one cell of a 64 pixel position-sensitive photomultiplier (Hamamatsu H-4139-20). Ambiguities in the hit combinations are resolved by using the segmented scintillators in front of and behind the hodoscopes.

The FPS detectors measure space points with a resolution of $\sigma_x = \sigma_y = 100 \mu\text{m}$. There is no magnetic field between the FPS detectors and the space points measured at 81 and 90 m are used to define a track at 85 m. In both stations, ten out of the 20 layers have to show signals, in coincidence with trigger tiles, in order to reconstruct a track. The efficiency for a minimum ionizing particle to produce a hit in a layer is typically 60% and the track reconstruction efficiency is approximately 50%. With the help of the transfer matrices of the magnetic channel, which are known with high accuracy between the interaction point and 85 m, trajectories are traced back to the interaction point and momenta are determined. Due to the fact that the HERA magnets lead to independent dispersion in both the horizontal and vertical planes, momenta can be measured twice by making use of the horizontal and vertical deflections. The two measurements have to agree within errors for tracks starting at the interaction point and this provides an efficient method for rejecting background tracks.

2.2 Calibration of the forward proton spectrometer

In order to reconstruct momenta, the coordinates and slopes of scattered proton trajectories are transformed into a reference system with the beam direction as the primary axis. As the actual beam position is not known with the required accuracy of 0.5 mm, the actual beam orbit is determined for each fill using the nominal orbit as the first

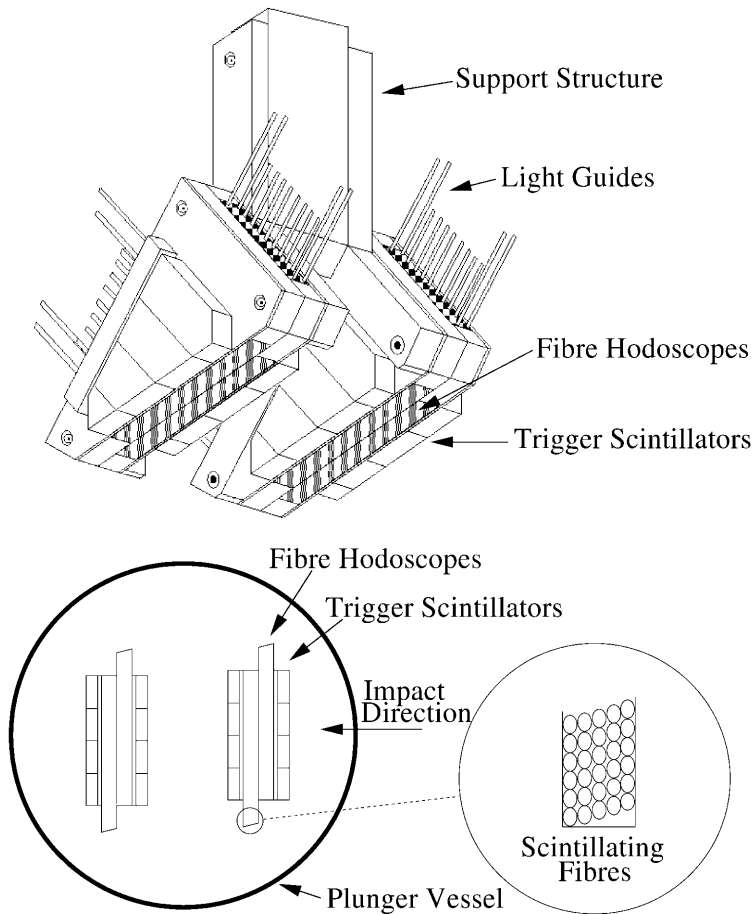


Fig. 1. Top: perspective view of the scintillating fibre hodoscopes and the trigger scintillators inside a Roman Pot. Bottom: horizontal cross section through one FPS station

approximation. First the offset and tilt of the actual beam orbit with respect to the nominal one are determined in the horizontal plane by a fit that makes use of the fact that certain combinations of impact points and slopes at 85 m are ‘forbidden’ for particles coming from the nominal interaction vertex [22]. For the calibration of the momentum measurement in the vertical plane, the difference between horizontal and vertical momentum measurements is used as additional input. Only protons, for which the momentum error arising from the uncertainty of the calibration in the horizontal plane is small, are used for this purpose. This procedure, which has been verified by Monte Carlo simulations of the FPS, leads to a momentum resolution of typically $\sigma(E'_p) = 6 \text{ GeV}$ at 700 GeV. The angular resolution at the interaction point is $\sigma(\theta_x) = 5 \mu\text{rad}$, while $\sigma(\theta_y)$ varies between 5 and 100 μrad depending upon energy and angle. The calibration of the FPS is described in more detail in [23].

The FPS calibration was checked using high- Q^2 DIS events with a forward rapidity gap [22]. For events with these characteristics the hadronic final state is well contained within the central H1 detectors and one can compare the observed missing longitudinal momentum with the one measured by the FPS assuming that no particles escape in the forward region. The mean difference between the proton energy measured in the FPS and the energy ex-

pected from the calorimetric measurement is $(-1 \pm 9) \text{ GeV}$. From this we conclude that the scale of the FPS energy measurement is correct to within 10 GeV.

2.3 Detection of leading neutrons

During 1996 the H1 experiment used a forward neutron calorimeter constructed of lead and scintillating fibres. The calorimeter, which was originally used by the WA89 experiment [24–26] at CERN, weighs approximately 10 tons and is located 107 m away from the nominal H1 interaction point. Final state neutrons with production angles $\theta \lesssim 0.5 \text{ mrad}$ are within the acceptance of the FNC. A schematic diagram of the FNC is shown in Fig. 2.

The forward neutron calorimeter consists of interleaved layers of 2 m long lead strips and scintillating fibres. The lead to fibre volume ratio is 4:1 and the nuclear interaction-length λ_I is 21 cm. The calorimeter is laterally segmented into hexagonal modules each of which is defined by coupling 1141 scintillating fibres to a common photomultiplier located at the rear of the detector. The height of a hexagonal module is 8.6 cm. A gap between the top and bottom parts of the calorimeter is necessary in order to have space for the proton beam pipe which passes through the calorimeter. There are 67 modules in

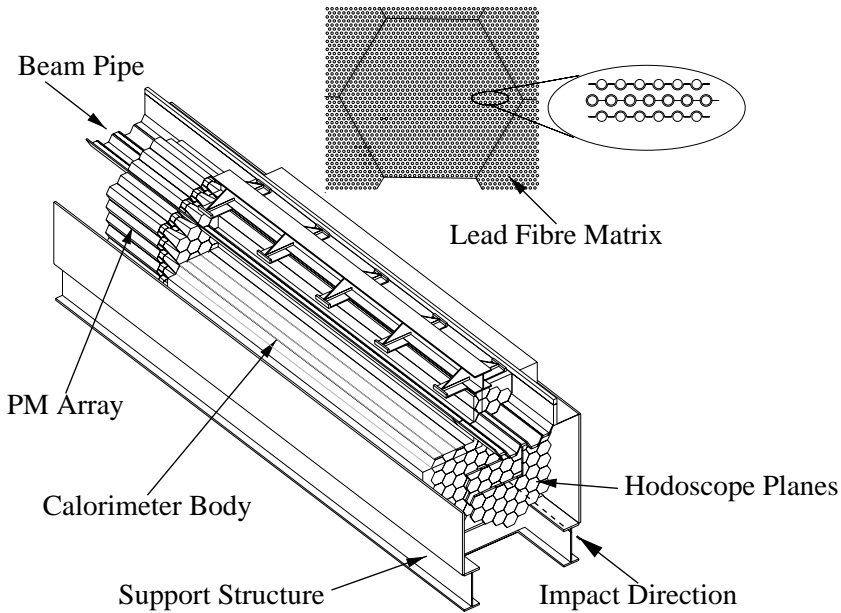


Fig. 2. Configuration of the H1 forward neutron calorimeter. The calorimeter consists of interleaved layers of lead and scintillating fibres. A hexagonal module, see inset, is defined by coupling 1141 scintillating fibres to a common photomultiplier located at the rear of the detector

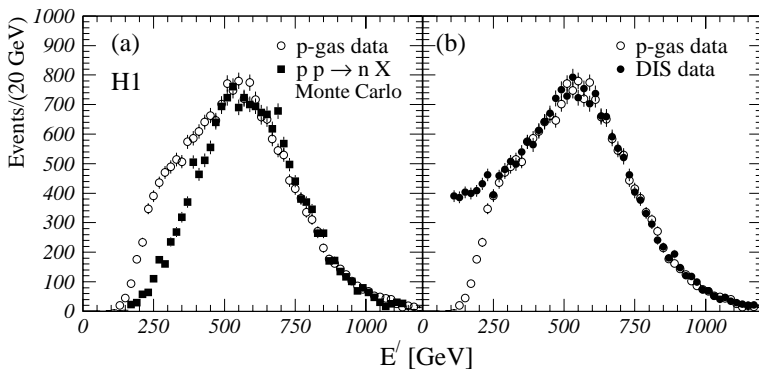


Fig. 3. **a** The observed neutron energy spectrum in proton beam-gas interactions compared to the results of a $pp \rightarrow nX$ Monte Carlo simulation based upon pion exchange. The Monte Carlo simulates the acceptance and response of the FNC. **b** The same proton beam-gas energy spectrum compared to the neutron energy distribution observed in DIS interactions. The proton beam-gas energy spectrum has not been corrected for the trigger efficiency which is less than 100% below 300 GeV. All distributions are normalized to the number of events with $E' \geq 500$ GeV

the bottom part of the calorimeter and eight modules in the top part.

The scintillating fibres are 1 mm in diameter and are orientated approximately parallel to the direction of the incident neutron. The attenuation length of the scintillating fibres is (1.7 ± 0.2) m which has been measured using muons from cosmic events. Detailed GEANT [27] simulation studies have shown that this small attenuation length is responsible for the high-energy tail (see Fig. 3) that we observe in the neutron energy spectra. The high-energy tail is due to fluctuations in the longitudinal shower profile which lead to energy depositions close to the back-end of the calorimeter. Because of the small distance to the photomultipliers, the produced scintillation light is attenuated less than normal leading to an over-estimation of the incident particle's energy. The energy resolution of the calorimeter is $\sigma(E)/E \approx 20\%$ for energies between 300 and 800 GeV.

Two segmented planes of hodoscopes situated in front of the FNC are used to veto charged particles. Each plane is constructed of 1 cm thick hexagonal scintillator tiles which have the same lateral size as the calorimeter modules. The neutron detection efficiency of the FNC is $(93 \pm$

5)%), the losses being due to coincidences in the veto hodoscopes which mostly originate from the back-scattering of charged particles produced during the neutron's hadronic shower. This efficiency was determined by measuring the rate of signals in the hodoscopes as a function of the radial distance away from the neutron impact position reconstructed in the calorimeter. Extrapolating the rate of signals in the hodoscopes to the region close to the impact position, the probability due to back-scattering was estimated.

In this analysis we assume that all neutral clusters are produced by neutrons. Using the LEPTO Monte Carlo program [11] and a GEANT [27] simulation of the H1 beam line, we estimate that the background contribution due to other neutral particles (mostly photons and K_L^0) is 6% for events with $z > 0.2$. For $z > 0.6$, the background contribution is 2%.

All detector components, including the calorimeter and the hodoscope planes, are covered with lead sheets in order to shield them from synchrotron radiation.

2.4 Calibration of the forward neutron calorimeter

The 75 modules of the FNC were initially calibrated at CERN using a 10 GeV incident electron beam. The FNC was positioned on a movable platform which allowed the response of each module to be measured separately. Preliminary calibration constants for the entire FNC were then determined by a matrix inversion procedure [28]. After this initial calibration, the FNC had an approximately uniform response independent of impact position.

After the calorimeter was installed in the H1 beam line, run-dependent calibration constants were determined every few weeks by comparing the high-energy spectrum of neutrons, observed in interactions between the proton beam and residual gas in the beam pipe, with the results of a $pp \rightarrow nX$ Monte Carlo simulation based upon pion exchange [29]. Hadronic $pp \rightarrow nX$ data in the high z and low p_T range, obtained at the ISR and by other experiments at CERN [30,31], are well described by pion exchange and have been used to constrain the pion flux factor [8, 32]. Since the pion flux factor determines the high-energy spectrum of final-state neutrons, by comparing with the Monte Carlo simulation we are effectively calibrating the FNC with respect to previous experimental results. In the $pp \rightarrow nX$ Monte Carlo program, the acceptance and the energy response of the FNC are simulated by tracking neutrons through the GEANT [27] simulation of the H1 beam line.

Figure 3a shows the uncorrected neutron energy spectrum observed in proton beam–gas interactions compared to the results of the Monte Carlo simulation. The two distributions are normalized to the same number of entries above 500 GeV. The peak position and the high-energy tail observed in the data are in good agreement with the simulation. Since the rate of neutron production with $z < 0.5$ is known to be underestimated by pion exchange [32], we do not use proton beam–gas data in this energy range for calibration purposes. This comparison, between proton beam–gas interactions and the pion exchange Monte Carlo simulation, is the method we use to calibrate the FNC. We estimate a 5% energy scale uncertainty for the FNC based upon our comparison between proton beam–gas interactions and the pion exchange Monte Carlo simulation.

Figure 3b shows the same beam–gas energy spectrum compared to the neutron energy spectrum observed in DIS interactions. Above 300 GeV the two distributions again agree very well in shape. This agreement supports the hypothesis that the pion flux factor is a universal property of the proton which is the same in both DIS and hadronic interactions [7,8]. Below 300 GeV, the sharp rise in the proton beam–gas energy spectrum is due to the trigger threshold used to obtain the data.

The short-term gain variation of the FNC photomultipliers is measured by a light-emitting diode (LED) monitoring system [28]. The light from seven LEDs is coupled by optical fibres to the entrance windows of all the photomultipliers. The average response of the FNC photomultipliers to the LED light is used on a run-by-run basis to correct for small changes in the gain of the FNC pho-

tomultipliers. When there are stable beam conditions, the gain variation of the FNC photomultipliers is typically less than 0.1% during 30 min.

The spatial resolution of the FNC was determined using charged particles and three small scintillator counters situated in front of the calorimeter. The scintillators are $3 \times 3 \times 10 \text{ mm}^3$ and they are used in coincidence with a hodoscope tile to define a trigger. The spatial resolution of the FNC was determined to be:

$$\sigma_{xy}(E) = \left(\frac{5.13 \pm 0.81}{\sqrt{E [\text{GeV}]}} + (0.22 \pm 0.07) \right) \text{ cm}, \quad (6)$$

where the reconstructed impact position was determined using the centre-of-gravity of the hadronic shower and an empirical formula which corrects for the hexagonal shape of the calorimeter modules [28,33].

3 Event selection and data analysis

The final-state proton and neutron data used to measure the semi-inclusive structure functions were collected during different years. The proton data were obtained during 1995 using a trigger which required a charged track through both detector stations of the FPS and a localized cluster in the backward (SPACAL) electromagnetic calorimeter. For part of the data a track candidate in the central jet chamber was also required by the trigger. During 1996, a trigger which required an energy deposit in the SPACAL electromagnetic calorimeter and the absence of out-of-time background signals was used to obtain the DIS data containing a high-energy neutron.

During the offline analysis selection, criteria were applied to the data in order to reduce beam-related backgrounds, events due to photoproduction and events from reactions in which the incoming positron lost a significant amount of energy by radiation. The DIS selection criteria used in the analysis are:

- A positron with energy $E'_e \geq 12 \text{ GeV}$ in the angular range $156^\circ \leq \theta_e \leq 177^\circ$ was required which ensures that the scattered positron is within the acceptance region of the SPACAL electromagnetic calorimeter.
- The DIS kinematic variables were required to be in the range $2 \leq Q^2 \leq 50 \text{ GeV}^2$, $0.02 \leq y \leq 0.6$ and $6 \times 10^{-5} \leq x \leq 6 \times 10^{-3}$. The kinematic variables are reconstructed using the Σ method [34] which combines the scattered positron energy and angle measurements with the quantity Σ , which is the sum over all hadronic final-state particles of the differences between energy and longitudinal momentum. The Σ method has good resolution and keeps radiative corrections small over the entire kinematic range considered here.
- The quantity $\sum_i (E_i - p_{z,i})$, which is calculated using the energy E_i and the longitudinal momentum $p_{z,i}$ of all final-state particles including the scattered positron, is expected to be twice the electron beam energy. This quantity was required to be $\geq 40 \text{ GeV}$ for the neutron analysis and $\geq 41.6 \text{ GeV}$ for the proton analysis. These cuts suppress radiative events and photoproduction background.

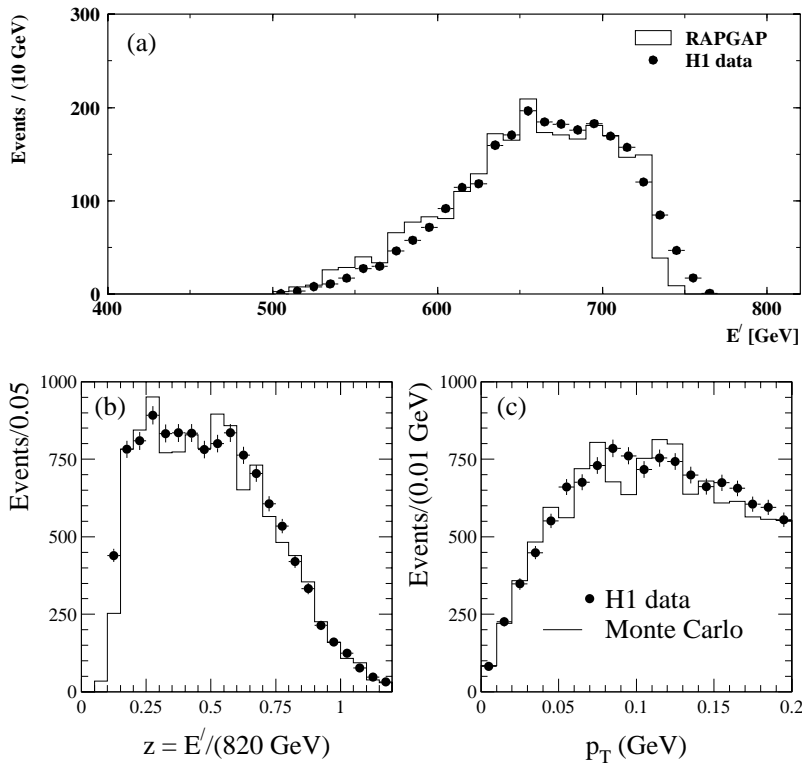


Fig. 4. **a** The observed proton energy spectrum compared to a simulation based upon the RAPGAP Monte Carlo generator. In **b** and **c** the observed neutron z and p_T spectra, integrated over the entire kinematic range in x and Q^2 , are compared to reweighted Monte Carlo data which result from the unfolding procedure used to correct the data for acceptance and migration effects. The Monte Carlo distributions are normalized to the total number of events in the data

- The reconstructed vertex position was required to be within ± 30 cm of the nominal vertex position in z .
- The proton analysis required at least one central track in the CJC with $p_T \geq 450$ MeV to originate from the interaction vertex.

Cuts related to the final-state baryons are:

- For the proton data, one forward track with $580 \leq E'_p \leq 740$ GeV and $p_T \leq 200$ MeV was required to be detected by the FPS. Fiducial cuts on θ_x and θ_y , which depended on the proton energy, were applied to ensure that the track was observed in a region of the phase space where the acceptance was well understood and stable over the run period.
- For the neutron data, one neutral cluster with $E'_n \geq 100$ GeV and $p_T \leq 200$ MeV was required to be reconstructed in the FNC.

After these cuts the data samples were grouped into 12 (x, Q^2) bins in the range $6 \times 10^{-5} \leq x \leq 6 \times 10^{-3}$ and $2 \leq Q^2 \leq 50$ GeV². The proton data sample consists of 1661 events and the neutron data consists of 10 366 events. The total luminosities of the proton and neutron data samples are (1.44 ± 0.03) pb⁻¹ and (3.38 ± 0.07) pb⁻¹ respectively.

The acceptances of the FPS and the FNC were determined by Monte Carlo programs in which protons or neutrons from DIS reactions were tracked through a simulation of the HERA beam line. The finite aperture of the beam line magnets limits the acceptance of both the FPS and the FNC.

The FPS acceptance as a function of z was calculated using the RAPGAP Monte Carlo program which simulates

pion exchange [35]. This Monte Carlo simulation gives a good description of the shape of the uncorrected data as shown in Fig. 4a for the observed proton energy spectrum. The FPS acceptance is approximately 80% for protons with $0.76 \leq z \leq 0.90$ and $p_T \leq 200$ MeV. The LEPTO and ARIADNE [36] Monte Carlo programs were used to check that the FPS acceptance is independent of the assumed production model and to estimate the systematic uncertainties.

The corrected neutron energy spectrum was determined separately in each (x, Q^2) bin by using an unfolding procedure [37]. The procedure uses Monte Carlo events to simultaneously correct the observed FNC energy spectrum for acceptance and migration effects. The LEPTO and RAPGAP Monte Carlo models were used to demonstrate that the unfolded neutron energy spectrum does not depend upon the production model used to correct the data. For neutrons with $z \geq 0.4$ and $p_T \leq 200$ MeV the FNC acceptance is $\gtrsim 30\%$.

Figures 4b and 4c show the observed neutron z and p_T spectra compared to the reweighted Monte Carlo simulation which results from the unfolding procedure. The data and Monte Carlo distributions, shown in Fig. 4b, are in agreement by construction since the unfolding procedure does a fit to the data by reweighting the Monte Carlo as a function of z . The p_T distributions, shown in Fig. 4c, demonstrate that the reweighted Monte Carlo gives a good description of a variable not used in the fit.

The semi-inclusive structure functions $F_2^{LP(3)}$ and $F_2^{LN(3)}$ have been corrected to the Born level. Radiative corrections were calculated using the program HERACLES [38]. In all (x, Q^2) bins they are smaller than

6%. We have included a 2% systematic error on our radiative corrections due to hadronic corrections and higher-order processes which are not simulated by the HERACLES code.

There are three types of systematic errors: normalization errors, errors which depend on the final-state baryons and errors which are different for each (x, Q^2) bin:

- Normalization systematic errors
 - For the proton analysis the normalization error is 5.6%. The main contribution to this error is the 5.0% uncertainty in the proton reconstruction efficiency.
 - The normalization error for the neutron analysis is 5.7%. The 5.4% uncertainty in the neutron detection efficiency is the largest component of this error.

The systematic errors on the total integrated luminosities, which are approximately 2%, are included in the normalization uncertainties.

- Final-state baryon systematic errors
 - For the proton analysis, these errors are between 4.8% and 19%. Errors in the migration corrections for the proton energy intervals, which depend on the accuracy of the calibration procedure, were evaluated from Monte Carlo studies and range between 4.5% and 19% for the different bins. Additional errors due to the uncertainty in the acceptance of the fiducial cuts were evaluated by comparing the results obtained using the RAPGAP, LEPTO and ARIADNE Monte Carlo models.
 - The FNC energy spectrum, after being corrected for acceptance and migration effects by using the unfolding procedure, has large systematic errors. We have varied the FNC energy scale by $\pm 5\%$ and reweighted the Monte Carlo data as a function of p_T to estimate these systematic errors. We have also used the shape of the impact point distribution and its maximum, which defines the zero degree direction, to determine the FNC acceptance. A systematic error is applied corresponding to the difference between this acceptance method and the acceptance determined using the unfolding procedure. These uncertainties lead to systematic errors which range between 16% and 58% for the corrected neutron energy spectrum.
- Errors which depend on x and Q^2
 - The systematic errors which differ in each (x, Q^2) bin range between 7.7% and 13% for the proton analysis. The uncertainties in the trigger efficiency and in the corrections for migrations between different bins in x and Q^2 are the main contributions to these systematic errors. The uncertainty in the acceptance and in the migrations as a function of x and Q^2 was determined by varying the energy scale of the SPACAL calorimeter by $\pm 1.5\%$, by varying the electron scattering angle by ± 1 mrad

and by simulating, according to our knowledge of the hadronic energy scale of the LAr calorimeter, a 4% uncertainty in the measurement of Σ .

- For the neutron analysis, the systematic errors which depend upon x and Q^2 range between 3.1% and 7.2%, since the measurement of the scattered positron was further improved in 1996. The main source of these systematic errors is the uncertainty in the acceptance and in the migrations as a function of x and Q^2 which was determined by varying the energy scale of the SPACAL calorimeter by between $\pm 1\%$ and $\pm 3\%$ (depending upon the energy of the scattered positron), by varying the reconstructed angle of the scattered positron by ± 0.5 mrad and by varying the energy scale of the LAr calorimeter by $\pm 4\%$.

These errors can be compared with the statistical ones. The statistical errors for the proton analysis lie between 9.6% and 30% for 90% of the data points. For the neutron analysis, the statistical errors range between 4.7% and 29% for 90% of the data points.

4 The semi-inclusive structure functions $F_2^{\text{LP}(3)}$ and $F_2^{\text{LN}(3)}$

Our measurement of the semi-inclusive structure functions $F_2^{\text{LP}(3)}$ and $F_2^{\text{LN}(3)}$, for leading protons and neutrons with $p_T \leq 200$ MeV, are shown in Figs. 5 and 6. The inner error bars show the statistical errors and the full error bars show the statistical and systematic errors added in quadrature. Tables 1 and 2 list the values of the semi-inclusive structure functions shown in the figures. The data are compared to the predictions of the LEPTO and RAPGAP Monte Carlo models [11,35].

The LEPTO 6.5 Monte Carlo program simulates baryon production using soft colour interactions and the JETSET string fragmentation model [11,14]. Soft colour interaction models have been proposed to explain large rapidity gap events and the production of final-state baryons [12,13]. In these models, the colour structure of the partons interacting with the virtual photon is modified by non-perturbative soft gluon exchanges which can lead to the production of colour neutral partonic subsystems separated in rapidity. After the fragmentation process, a high-energy baryon may be produced separated by a large rapidity gap from the remainder of the hadronic final state.

The LEPTO Monte Carlo model describes the general shape and magnitude of the neutron data over the entire z range. It fails, however, to describe the rate of leading proton production and the rise in $F_2^{\text{LP}(3)}$ as a function of Q^2 . The leading order parton distributions for the proton by Glück, Reya and Vogt (GRV) [39,40], and the default value of 0.5 as the probability for soft colour interactions, were used to calculate the LEPTO Monte Carlo predictions.

The RAPGAP Monte Carlo program simulates leading baryon production using pion exchange. In the Monte Carlo program, the cross sections for leading proton and

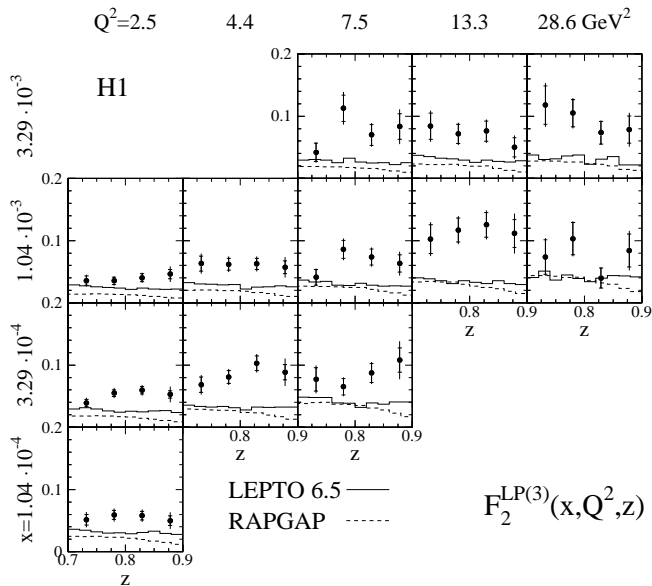


Fig. 5. Measurement of $F_2^{\text{LP}(3)}$, for protons with $p_T \leq 200$ MeV, compared to the predictions of the LEPTO and RAPGAP Monte Carlo models calculated using GRV leading order parton distributions for the proton and the pion respectively. The inner error bars show the statistical errors and the full error bars show the statistical and systematic errors added in quadrature. There is an additional 5.6% overall normalization uncertainty for the data points which has not been included in the full error bars

neutron production are proportional to the product of the pion flux factor and the pion structure function. The pion flux factor determines the energy and p_T spectra of the final-state baryons and is identical for proton and neutron production except for a factor of two. For the RAPGAP Monte Carlo predictions shown in Figs. 5 and 6 we have used the pion flux factor determined by Holtmann et al. [8]. The rate of leading baryon production depends also upon the values of the pion parton distributions and we have used the leading order parametrization by GRV [39, 40].

The RAPGAP Monte Carlo program gives a reasonable description of the high-energy neutron data with $z \geq 0.7$ but it fails to reproduce the absolute rate of proton production. In the low-energy region where the final-state neutron has $<70\%$ of the incident proton's energy, the RAPGAP Monte Carlo program is not valid since additional physical processes, not simulated by the program, are expected to contribute significantly to the production of neutrons.

It is interesting to compare the magnitudes of $F_2^{\text{LP}(3)}$ and $F_2^{\text{LN}(3)}$. For $z \geq 0.7$, the semi-inclusive cross section for proton production is larger than the cross section for neutron production in any specific (x, Q^2) bin. This result rules out pion exchange as the main production mechanism for leading protons since pion exchange models predict that the ratio of neutron and proton production should be equal to two.

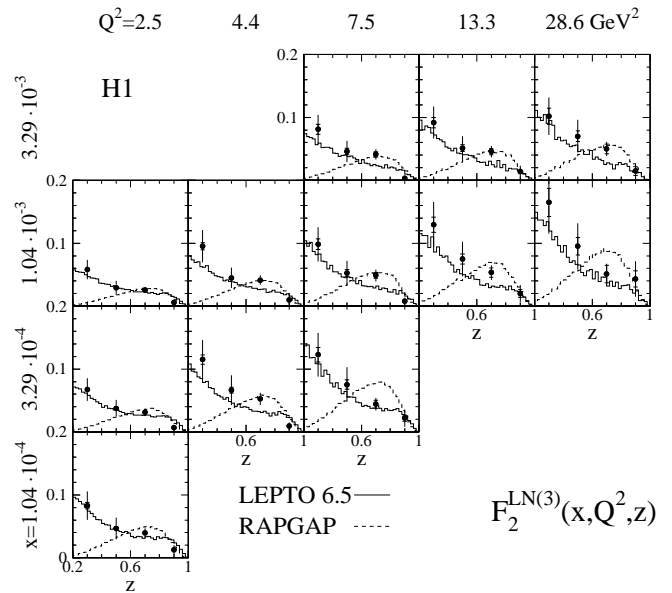


Fig. 6. The semi-inclusive structure function $F_2^{\text{LN}(3)}$, for neutrons with $p_T \leq 200$ MeV, compared to the predictions of the LEPTO and RAPGAP Monte Carlo models calculated using GRV leading order parton distributions for the proton and the pion respectively. The inner error bars show the statistical errors and the full error bars show the statistical and systematic errors added in quadrature. There is an additional 5.7% overall normalization uncertainty for the data points which has not been included in the full error bars

5 Factorization and scaling violations of $F_2^{\text{LP}(3)}$ and $F_2^{\text{LN}(3)}$

Presuming that leading baryons emerge from reactions where the virtual photon is absorbed by a colourless object inside the proton, the structure function $F_2^{\text{LB}(3)}$ should factorize into a flux factor $f(z)$ which is only a function of z , and a structure function $F_2^{\text{LB}(2)}$ which depends upon β and Q^2 . The quantity $\beta = x/(1-z)$ may be interpreted as the fraction of the exchanged object's momentum carried by the quark or gluon interacting with the virtual photon.

Alternatively one may assume models [12] which are not based on the exchange of colourless objects so that β can no longer be interpreted as a momentum fraction. In such scenarios, one might expect factorization in the variables x , Q^2 and z , if the deep-inelastic scattering process off the proton is independent of the proton fragmentation. The 'hypothesis of limiting fragmentation' [41], which states that target fragmentation is independent of the incident projectile's energy, also implies that final-state baryons emerge from a process which is insensitive to x and Q^2 .

To test both factorization hypotheses, fits were made to the proton and neutron data separately assuming the following general forms for $F_2^{\text{LB}(3)}$ [23, 29]:

Table 1. The measured values of $F_2^{\text{LP}(3)}(x, Q^2, z)$ for protons with $p_T \leq 200$ MeV. There is an additional normalization uncertainty of 5.6% not included in the systematic error

| x | Q^2 [GeV ²] | z | $F_2^{\text{LP}(3)} \pm \text{stat.} \pm \text{syst.}$ | x | Q^2 [GeV ²] | z | $F_2^{\text{LP}(3)} \pm \text{stat.} \pm \text{syst.}$ |
|---------|---------------------------|-------|--|---------|---------------------------|-------|--|
| 0.00010 | 2.5 | 0.732 | $0.0514 \pm 0.0086 \pm 0.0087$ | 0.00104 | 7.5 | 0.732 | $0.0411 \pm 0.0125 \pm 0.0064$ |
| 0.00010 | 2.5 | 0.780 | $0.0590 \pm 0.0072 \pm 0.0079$ | 0.00104 | 7.5 | 0.780 | $0.0859 \pm 0.0143 \pm 0.0100$ |
| 0.00010 | 2.5 | 0.829 | $0.0580 \pm 0.0071 \pm 0.0073$ | 0.00104 | 7.5 | 0.829 | $0.0736 \pm 0.0131 \pm 0.0079$ |
| 0.00010 | 2.5 | 0.878 | $0.0499 \pm 0.0076 \pm 0.0112$ | 0.00104 | 7.5 | 0.878 | $0.0631 \pm 0.0139 \pm 0.0136$ |
| 0.00033 | 2.5 | 0.732 | $0.0392 \pm 0.0058 \pm 0.0059$ | 0.00329 | 7.5 | 0.732 | $0.0419 \pm 0.0148 \pm 0.0073$ |
| 0.00033 | 2.5 | 0.780 | $0.0550 \pm 0.0054 \pm 0.0060$ | 0.00329 | 7.5 | 0.780 | $0.1126 \pm 0.0209 \pm 0.0157$ |
| 0.00033 | 2.5 | 0.829 | $0.0595 \pm 0.0057 \pm 0.0060$ | 0.00329 | 7.5 | 0.829 | $0.0699 \pm 0.0167 \pm 0.0093$ |
| 0.00033 | 2.5 | 0.878 | $0.0528 \pm 0.0061 \pm 0.0112$ | 0.00329 | 7.5 | 0.878 | $0.0832 \pm 0.0205 \pm 0.0191$ |
| 0.00104 | 2.5 | 0.732 | $0.0357 \pm 0.0076 \pm 0.0058$ | 0.00104 | 13.3 | 0.732 | $0.1024 \pm 0.0230 \pm 0.0150$ |
| 0.00104 | 2.5 | 0.780 | $0.0354 \pm 0.0059 \pm 0.0045$ | 0.00104 | 13.3 | 0.780 | $0.1168 \pm 0.0193 \pm 0.0121$ |
| 0.00104 | 2.5 | 0.829 | $0.0403 \pm 0.0064 \pm 0.0048$ | 0.00104 | 13.3 | 0.829 | $0.1253 \pm 0.0200 \pm 0.0118$ |
| 0.00104 | 2.5 | 0.878 | $0.0461 \pm 0.0076 \pm 0.0102$ | 0.00104 | 13.3 | 0.878 | $0.1114 \pm 0.0222 \pm 0.0233$ |
| 0.00033 | 4.4 | 0.732 | $0.0684 \pm 0.0123 \pm 0.0098$ | 0.00329 | 13.3 | 0.732 | $0.0839 \pm 0.0211 \pm 0.0141$ |
| 0.00033 | 4.4 | 0.780 | $0.0807 \pm 0.0102 \pm 0.0080$ | 0.00329 | 13.3 | 0.780 | $0.0715 \pm 0.0153 \pm 0.0094$ |
| 0.00033 | 4.4 | 0.829 | $0.1030 \pm 0.0117 \pm 0.0092$ | 0.00329 | 13.3 | 0.829 | $0.0759 \pm 0.0164 \pm 0.0094$ |
| 0.00033 | 4.4 | 0.878 | $0.0887 \pm 0.0123 \pm 0.0183$ | 0.00329 | 13.3 | 0.878 | $0.0500 \pm 0.0153 \pm 0.0112$ |
| 0.00104 | 4.4 | 0.732 | $0.0631 \pm 0.0121 \pm 0.0107$ | 0.00104 | 28.6 | 0.732 | $0.0737 \pm 0.0279 \pm 0.0111$ |
| 0.00104 | 4.4 | 0.780 | $0.0619 \pm 0.0094 \pm 0.0083$ | 0.00104 | 28.6 | 0.780 | $0.1030 \pm 0.0259 \pm 0.0112$ |
| 0.00104 | 4.4 | 0.829 | $0.0626 \pm 0.0091 \pm 0.0079$ | 0.00104 | 28.6 | 0.829 | $0.0398 \pm 0.0163 \pm 0.0039$ |
| 0.00104 | 4.4 | 0.878 | $0.0572 \pm 0.0101 \pm 0.0129$ | 0.00104 | 28.6 | 0.878 | $0.0840 \pm 0.0266 \pm 0.0178$ |
| 0.00033 | 7.5 | 0.732 | $0.0770 \pm 0.0189 \pm 0.0121$ | 0.00329 | 28.6 | 0.732 | $0.1179 \pm 0.0307 \pm 0.0171$ |
| 0.00033 | 7.5 | 0.780 | $0.0652 \pm 0.0132 \pm 0.0077$ | 0.00329 | 28.6 | 0.780 | $0.1047 \pm 0.0220 \pm 0.0106$ |
| 0.00033 | 7.5 | 0.829 | $0.0873 \pm 0.0151 \pm 0.0096$ | 0.00329 | 28.6 | 0.829 | $0.0734 \pm 0.0184 \pm 0.0067$ |
| 0.00033 | 7.5 | 0.878 | $0.1080 \pm 0.0197 \pm 0.0234$ | 0.00329 | 28.6 | 0.878 | $0.0784 \pm 0.0219 \pm 0.0163$ |

Table 2. The measured values of $F_2^{\text{LN}(3)}(x, Q^2, z)$ for neutrons with $p_T \leq 200$ MeV. There is an additional normalization uncertainty of 5.7% not included in the systematic error

| x | Q^2 [GeV ²] | z | $F_2^{\text{LN}(3)} \pm \text{stat.} \pm \text{syst.}$ | x | Q^2 [GeV ²] | z | $F_2^{\text{LN}(3)} \pm \text{stat.} \pm \text{syst.}$ |
|---------|---------------------------|-----|--|---------|---------------------------|-----|--|
| 0.00010 | 2.5 | 0.3 | $0.0829 \pm 0.0051 \pm 0.0219$ | 0.00104 | 7.5 | 0.3 | $0.0984 \pm 0.0085 \pm 0.0259$ |
| 0.00010 | 2.5 | 0.5 | $0.0470 \pm 0.0033 \pm 0.0165$ | 0.00104 | 7.5 | 0.5 | $0.0527 \pm 0.0054 \pm 0.0184$ |
| 0.00010 | 2.5 | 0.7 | $0.0396 \pm 0.0030 \pm 0.0068$ | 0.00104 | 7.5 | 0.7 | $0.0488 \pm 0.0047 \pm 0.0082$ |
| 0.00010 | 2.5 | 0.9 | $0.0125 \pm 0.0023 \pm 0.0073$ | 0.00104 | 7.5 | 0.9 | $0.0080 \pm 0.0029 \pm 0.0046$ |
| 0.00033 | 2.5 | 0.3 | $0.0673 \pm 0.0032 \pm 0.0176$ | 0.00329 | 7.5 | 0.3 | $0.0812 \pm 0.0079 \pm 0.0213$ |
| 0.00033 | 2.5 | 0.5 | $0.0378 \pm 0.0020 \pm 0.0132$ | 0.00329 | 7.5 | 0.5 | $0.0458 \pm 0.0051 \pm 0.0160$ |
| 0.00033 | 2.5 | 0.7 | $0.0315 \pm 0.0018 \pm 0.0052$ | 0.00329 | 7.5 | 0.7 | $0.0412 \pm 0.0043 \pm 0.0069$ |
| 0.00033 | 2.5 | 0.9 | $0.0066 \pm 0.0013 \pm 0.0038$ | 0.00329 | 7.5 | 0.9 | $0.0033 \pm 0.0028 \pm 0.0019$ |
| 0.00104 | 2.5 | 0.3 | $0.0582 \pm 0.0034 \pm 0.0152$ | 0.00104 | 13.3 | 0.3 | $0.1295 \pm 0.0121 \pm 0.0341$ |
| 0.00104 | 2.5 | 0.5 | $0.0296 \pm 0.0021 \pm 0.0103$ | 0.00104 | 13.3 | 0.5 | $0.0749 \pm 0.0081 \pm 0.0262$ |
| 0.00104 | 2.5 | 0.7 | $0.0257 \pm 0.0019 \pm 0.0043$ | 0.00104 | 13.3 | 0.7 | $0.0533 \pm 0.0073 \pm 0.0090$ |
| 0.00104 | 2.5 | 0.9 | $0.0059 \pm 0.0013 \pm 0.0034$ | 0.00104 | 13.3 | 0.9 | $0.0202 \pm 0.0063 \pm 0.0117$ |
| 0.00033 | 4.4 | 0.3 | $0.1150 \pm 0.0073 \pm 0.0302$ | 0.00329 | 13.3 | 0.3 | $0.0918 \pm 0.0082 \pm 0.0242$ |
| 0.00033 | 4.4 | 0.5 | $0.0664 \pm 0.0047 \pm 0.0232$ | 0.00329 | 13.3 | 0.5 | $0.0512 \pm 0.0054 \pm 0.0179$ |
| 0.00033 | 4.4 | 0.7 | $0.0526 \pm 0.0039 \pm 0.0088$ | 0.00329 | 13.3 | 0.7 | $0.0457 \pm 0.0048 \pm 0.0077$ |
| 0.00033 | 4.4 | 0.9 | $0.0091 \pm 0.0028 \pm 0.0053$ | 0.00329 | 13.3 | 0.9 | $0.0141 \pm 0.0037 \pm 0.0082$ |
| 0.00104 | 4.4 | 0.3 | $0.0952 \pm 0.0055 \pm 0.0251$ | 0.00104 | 28.6 | 0.3 | $0.1650 \pm 0.0224 \pm 0.0444$ |
| 0.00104 | 4.4 | 0.5 | $0.0450 \pm 0.0035 \pm 0.0157$ | 0.00104 | 28.6 | 0.5 | $0.0952 \pm 0.0140 \pm 0.0337$ |
| 0.00104 | 4.4 | 0.7 | $0.0414 \pm 0.0030 \pm 0.0070$ | 0.00104 | 28.6 | 0.7 | $0.0509 \pm 0.0137 \pm 0.0091$ |
| 0.00104 | 4.4 | 0.9 | $0.0101 \pm 0.0019 \pm 0.0059$ | 0.00104 | 28.6 | 0.9 | $0.0433 \pm 0.0127 \pm 0.0253$ |
| 0.00033 | 7.5 | 0.3 | $0.1228 \pm 0.0116 \pm 0.0327$ | 0.00329 | 28.6 | 0.3 | $0.1018 \pm 0.0129 \pm 0.0267$ |
| 0.00033 | 7.5 | 0.5 | $0.0752 \pm 0.0075 \pm 0.0265$ | 0.00329 | 28.6 | 0.5 | $0.0702 \pm 0.0086 \pm 0.0245$ |
| 0.00033 | 7.5 | 0.7 | $0.0442 \pm 0.0064 \pm 0.0077$ | 0.00329 | 28.6 | 0.7 | $0.0499 \pm 0.0077 \pm 0.0084$ |
| 0.00033 | 7.5 | 0.9 | $0.0220 \pm 0.0050 \pm 0.0128$ | 0.00329 | 28.6 | 0.9 | $0.0148 \pm 0.0071 \pm 0.0086$ |

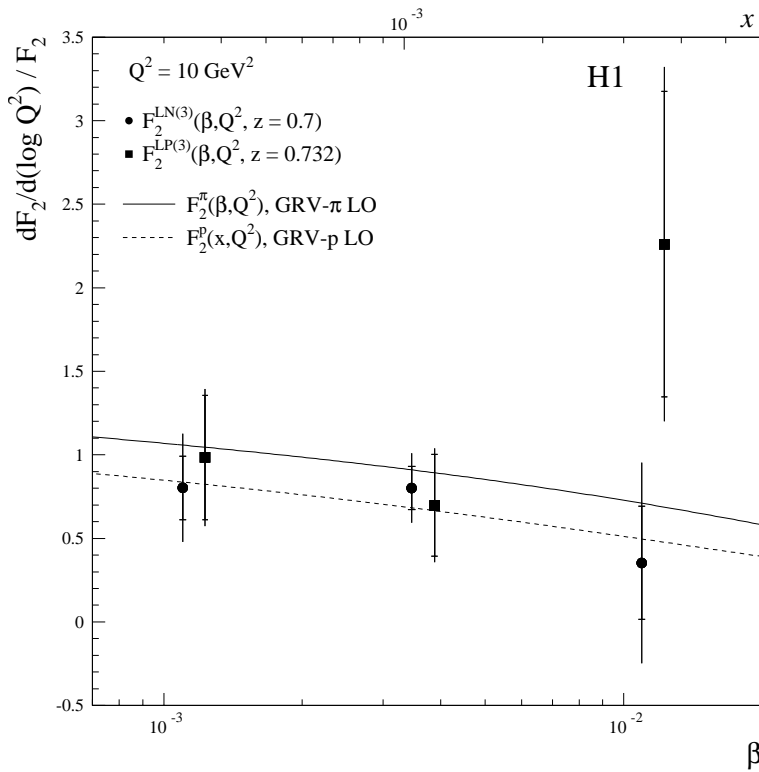


Fig. 7. Normalized scaling violations observed in the proton and neutron data, computed at $Q^2 = 10 \text{ GeV}^2$, compared to the expectations derived from GRV parametrizations of the inclusive structure functions for the pion and the proton. The scaling violations of the pion structure function have been evaluated as a function of β (lower scale), whereas for the proton structure function they have been evaluated as a function of x (upper scale)

$$F_2^{\text{LB}(3)}(\beta, Q^2, z) = f(z) \cdot F_2^{\text{LB}(2)}(\beta, Q^2) \quad (7)$$

$$F_2^{\text{LB}(3)}(x, Q^2, z) = f(z) \cdot F_2^{\text{LB}(2)}(x, Q^2), \quad (8)$$

where the discrete-function $f(z)$ is expressed by three free-parameters and for $F_2^{\text{LB}(2)}(\beta, Q^2)$ in (7) a functional form, based on the leading terms of a phenomenological parametrization of the proton structure function [42], was chosen. For $F_2^{\text{LB}(2)}(x, Q^2)$ in (8), β was replaced by x .

The data are consistent with both factorization hypotheses and the fit results yield similar χ^2/ndf . A possible explanation for this result is that $F_2^{\text{LB}(2)}$ is proportional to the proton structure function which for $x < 0.1$ is of the form $F_2 \sim x^{-\lambda(Q^2)}$ [42]. Since β and x are highly correlated and have similar magnitude due to the restricted range of z , this also implies that $F_2^{\text{LB}(2)} \sim \beta^{-\lambda(Q^2)}$. The data have therefore relatively limited sensitivity to a difference of factorization in these two variables.

In order to quantify the scaling violations observed in the data, $F_2^{\text{LP}(3)}$ and $F_2^{\text{LN}(3)}$ have been fitted separately for each fixed value of β to the form:

$$F_2^{\text{LB}(2)}(\beta, Q^2) = a(\beta) + b(\beta) \cdot \log Q^2, \quad (9)$$

with Q^2 in GeV^2 . The values of $b(\beta)/F_2^{\text{LB}(2)}$, which are a measure of the scaling violations, are plotted in Fig. 7. Only the fit results which arise from the proton data with $z = 0.732$ and the neutron data with $z = 0.7$ are shown since the results from the other z values are similar. The measurements of $F_2^{\text{LP}(3)}$ and $F_2^{\text{LN}(3)}$ in the lowest x bin have not been used since there is only a single Q^2 value. The data are compared to the scaling violations

$dF_2/d(\log Q^2)/F_2$ predicted and observed in the inclusive structure functions of the pion and proton respectively. The pion and proton structure functions have been calculated using the GRV leading order parametrizations [39, 40]. The scaling violations observed in the semi-inclusive structure functions $F_2^{\text{LP}(3)}$ and $F_2^{\text{LN}(3)}$ are similar in size and shape and are close to those seen in the GRV parametrizations of the pion and proton structure functions.

6 Comparison to a Regge model of baryon production

Assuming a simple Regge expansion and the dominance of a single Regge exchange, the differential cross section for leading baryon production as a function of z at fixed t should be proportional to $(1-z)^{-n}$. Here $n = 2\alpha(t) - 1$, and $\alpha(t)$ specifies the Regge trajectory of the dominant exchange. For the leading neutron data with $0.7 \leq z \leq 0.9$ shown in Fig. 6, the falling z spectra suggest a value of n , averaged over the t -dependence of the baryon production cross section, which is approximately equal to -1 . This implies that the average value of $\alpha(t)$ is consistent with zero which is naively the expectation of pion exchange. In contrast, the leading proton data, shown in Fig. 5, do not depend strongly on z so that the average value of $\alpha(t)$ is larger than the value suggested by the neutron data. This is consistent with the dominance of a trajectory with the intercept $\alpha(0) \simeq 0.5$ which was found to be the sub-leading contribution in the diffractive region at larger z [5].

Figure 8 shows a comparison between the leading baryon structure functions with $0.7 \leq z \leq 0.9$ and a Regge

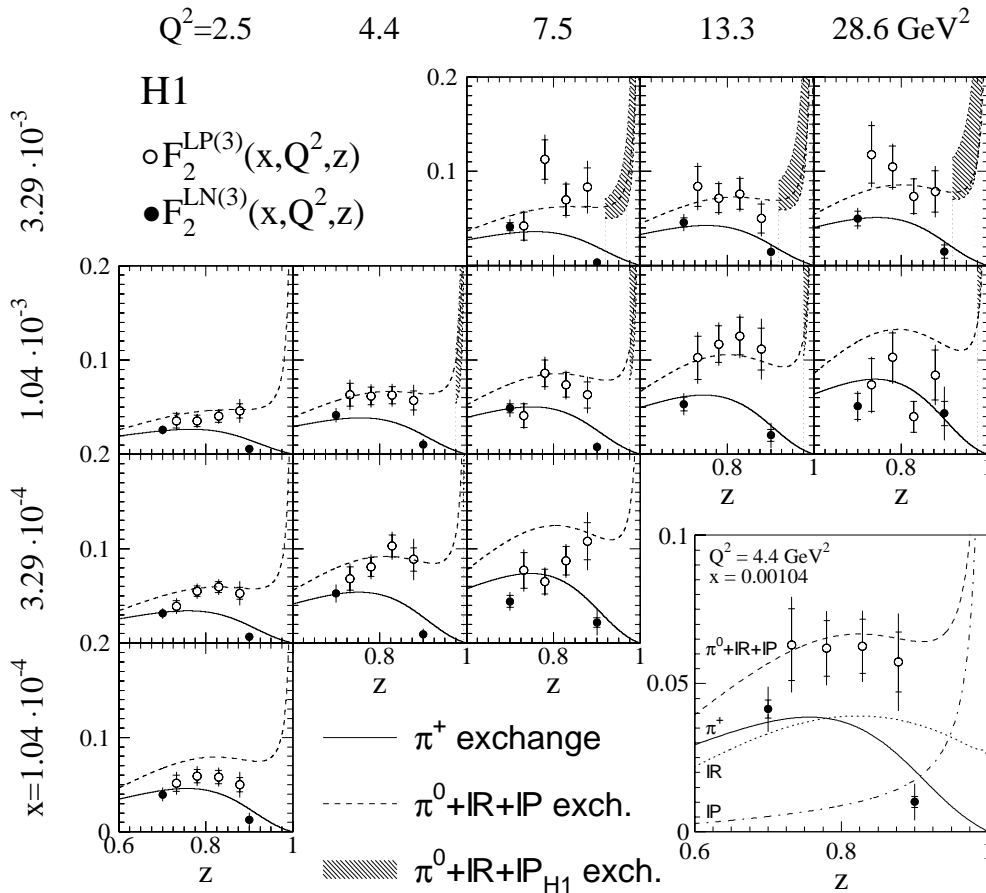


Fig. 8. The measured values of $F_2^{\text{LN}(3)}$ and $F_2^{\text{LP}(3)}$ with $z \geq 0.7$ compared to a Regge model of baryon production. The different contributions are labelled for the figure in the inset. The neutron data are described by π^+ exchange whereas the proton data are compared to the sum of π^0 , pomeron and secondary reggeon (f_2) exchanges. The π^0 contribution, which is not shown, is exactly half the π^+ contribution. The shaded band is explained in the text

model of baryon production. In the model, the contribution of a specific exchange i is determined by the product of its particle flux $f_{i/p}(z, t)$ and its structure function F_2^i evaluated at (β, Q^2) . For leading baryon production with $p_T \leq 200$ MeV we therefore have:

$$F_2^{\text{LB}(3)}(\beta, Q^2, z) = \sum_i \left(\int_{t_0}^{t_{\min}} f_{i/p}(z, t) dt \right) \times F_2^i(\beta, Q^2), \quad (10)$$

where i denotes the pion, the pomeron and secondary reggeons (for example ρ , ω , a_2 and f_2). The integration limits t_0 and t_{\min} are given by (5).

In the Regge model, we assume that the neutral pion, the pomeron and the f_2 all contribute to leading proton production. We neglect the contributions due to the other secondary reggeons because there is no sensitivity to them in the data, and because they have been estimated to be much smaller than the contribution due to f_2 exchange [43, 44]. A comparison of total hadronic cross section measurements has resulted in the estimate that the flux of reggeons which have isospin equal to one (ρ and a_2) is only $\approx 3\%$ of the flux of reggeons with isospin

equal to zero (ω and f_2) [43]. Regge phenomenology also predicts f_2 dominance, among isoscalar trajectories in the present case, in contrast to exchange degeneracy for elastic scattering processes [44].

For leading neutrons, we assume that they are produced by charged pion exchange only. In the limited p_T range of the data, leading neutron production due to ρ and a_2 exchanges has been estimated to be more than an order of magnitude smaller than the contribution due to pion exchange [9]. Pomeron exchange also does not give a significant contribution since neutron production due to diffractive dissociation is believed to be $\approx 6\%$ of the pion exchange contribution [9]. The present data sample has been used to estimate a 2% diffractive dissociation contribution to leading neutron production by determining the fraction of events with a large rapidity gap extending into the LAr calorimeter. We have neglected additional backgrounds such as neutron production due to resonance decays.

The pion, pomeron and reggeon flux factors have been determined using hadron-hadron data. The pion flux factor $f_{\pi/p}$ which we have used for neutron production is the

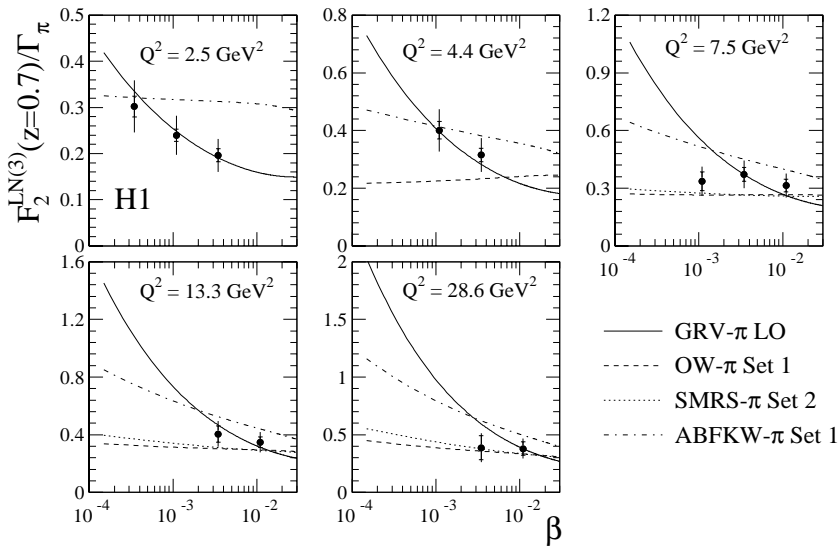


Fig. 9. $F_2^{\text{LN}(3)}/\Gamma_\pi$ at $z = 0.7$ plotted as a function of β for fixed values of Q^2 . The quantity Γ_π is the p_T integrated pion flux factor. Within the framework of the Regge model, $F_2^{\text{LN}(3)}/\Gamma_\pi$ can be interpreted as being equal to the pion structure function F_2^π . The data are compared to different parametrizations of F_2^π which are only shown in the Q^2 regions in which they are valid

same as the one used in [9]:

$$f_{\pi/p}(z, t) = C \frac{3g_{\pi Np}^2}{16\pi^2} (1-z)^{1-2\alpha'_\pi t} \times \frac{|t|}{(m_\pi^2 - t)^2} \exp\left(2R_\pi^2(t - m_\pi^2)\right), \quad (11)$$

where $g_{\pi Np}^2/(4\pi) = 13.6 \pm 0.3$ [45], $\alpha'_\pi = 1 \text{ GeV}^{-2}$, $R_\pi^2 = 0.3 \text{ GeV}^{-2}$ and the square of the Clebsch–Gordon coefficient is $C = 2/3$. For proton production via π^0 exchange we use the same flux factor with $C = 1/3$. The pomeron and reggeon flux factors are parameterized as [10, 43]:

$$f_{\mathbb{P}/p}(z, t) = \frac{54.4 \text{ GeV}^{-2}}{8\pi^2} \times (1-z)^{1-2\alpha_{\mathbb{P}}(t)} \exp\left(2R_{\mathbb{P}}^2 t\right) \quad (12)$$

$$f_{\mathbb{R}/p}(z, t) = \frac{390 \text{ GeV}^{-2}}{8\pi^2} \times (1-z)^{1-2\alpha_{\mathbb{R}}(t)} \exp\left(2R_{\mathbb{R}}^2 t\right), \quad (13)$$

where $\alpha_{\mathbb{P}}(t) = (1.08 + 0.25 \text{ GeV}^{-2} t)$ and $\alpha_{\mathbb{R}}(t) = (0.5 + 0.9 \text{ GeV}^{-2} t)$. The slopes are $R_{\mathbb{P}}^2 = 1.9 \text{ GeV}^{-2}$ and $R_{\mathbb{R}}^2 = 2 \text{ GeV}^{-2}$ respectively. The modulus squared of the reggeon signature factor¹, which is approximately equal to two, has been absorbed into the reggeon coupling and we have not included reggeon–pomeron interference terms in the model.

¹ In [10], (7) is missing the reggeon signature factor which is given in (5) of [43]. The two publications also use different values of $R_{\mathbb{R}}^2$. In [43], $R_{\mathbb{R}}^2 = 1.2 \text{ GeV}^{-2}$ which leads to a 12% difference in the values of the p_T -integrated reggeon flux factor at $z = 0.8$

The evaluation of the pion flux factor is not without some theoretical uncertainty. It has been pointed out that absorptive corrections, generated by double reggeon pion–pomeron exchanges, might play an important role in hadronic reactions in contrast to DIS. Since the pion flux factor which we have used was determined using $pp \rightarrow nX$ data, it might underestimate the flux of pions in the proton for DIS reactions by up to $\approx 30\%$ [46, 47].

The structure functions for the exchanged particles are basically unknown in the low β region and one has to rely on theoretical models. For the pion structure function F_2^π we took the leading order parametrization by Glück, Reya and Vogt [39, 40]. For the reggeon and pomeron structure functions we assume $F_2^{\mathbb{R}} = F_2^\pi$ and $F_2^{\mathbb{P}} = (0.026/0.12)F_2^{\mathbb{R}}$ following the arguments given in [10]. Measurements of the diffractive structure function $F_2^{\text{D}(3)}$ [3–6] only probe the pomeron at high β ($\beta > 0.04$) and it is not possible to use these data to fix the pomeron structure function $F_2^{\mathbb{P}}$ at the low β values of the semi-inclusive data ($\beta < 3 \times 10^{-3}$). In the small region of overlap, however, the QCD fits to $F_2^{\text{D}(3)}$ [5] are consistent with the pomeron model used in this paper as will be discussed below.

The model gives an acceptable description of the neutron and proton data with $0.7 \leq z \leq 0.9$, in view of the fact that all particle fluxes and structure functions were taken from the literature and that no adjustment was made. The rate of leading neutron production can be described entirely by π^+ exchange. However, proton production requires contributions from both f_2 and π^0 exchange which are roughly in the ratio 2:1 from the model.

The shaded band in Fig. 8 shows the prediction for $F_2^{\text{LP}(3)}$ in which we have replaced the pomeron component in our Regge model with the pomeron component determined using the QCD fit to $F_2^{\text{D}(3)}$ [5]. In the QCD fit, the pomeron structure function is parametrized at a low scale and evolved to larger Q^2 using the leading order DGLAP [48] equations. The hard-gluon leading order result which we have used for $F_2^{\mathbb{P}}$ (fit 3 in [5]) is only shown in the region in which it is valid ($3 \leq Q^2 \leq 75 \text{ GeV}^2$

and $0.04 \leq \beta \leq 1.0$) and it has been interpolated from $|t| \leq 1 \text{ GeV}^2$ to $p_T \leq 200 \text{ MeV}$ in order to allow comparison with the leading proton data. The width of the band reflects the uncertainty in the interpolation to the different kinematic region. The pomeron flux factor used in [5] has been evaluated using $\alpha_{\mathbb{P}}(t) = \alpha_{\mathbb{P}}(0) + \alpha'_{\mathbb{P}} t$, where $\alpha_{\mathbb{P}}(0) = 1.203 \pm 0.020 \text{ (stat.)} \pm 0.013 \text{ (syst.)}$ and $\alpha'_{\mathbb{P}} = (0.26 \pm 0.26) \text{ GeV}^{-2}$ [5]. The ZEUS measurement of the slope parameter $b = (7.2 \pm 1.1 \text{ (stat.)}^{+0.7}_{-0.9} \text{ (syst.)}) \text{ GeV}^{-2}$ [49], where $b = 2R_{\mathbb{P}}^2 - 2\alpha'_{\mathbb{P}} \ln(1-z)$, has also been used. This comparison demonstrates that the H1 measurements of $F_2^{\text{D}(3)}$ and $F_2^{\text{LP}(3)}$ can both be described by Regge phenomenology.

We use the measurement of $F_2^{\text{LN}(3)}$ at $z = 0.7$ and the integral of the pion flux factor to estimate the pion structure function at low Bjorken- x . Assuming that our Regge model of leading neutron production is valid, the quantity $F_2^{\text{LN}(3)}/\Gamma_{\pi}$ can be interpreted as being equal to the structure function of the pion where:

$$\Gamma_{\pi}(z = 0.7) = \int_{t_0}^{t_{\min}} f_{\pi/p}(z = 0.7, t) dt = 0.131. \quad (14)$$

Figure 9 shows $F_2^{\text{LN}(3)}/\Gamma_{\pi}$ as a function of β for fixed values of Q^2 . The data are compared to predictions of several parametrizations of the pion structure function [39, 40, 50–52]. The latter are only shown in the Q^2 regions in which they are valid. The data are in good agreement with the expectations of the GRV leading order parametrization of the pion structure function.

The quark and gluon distributions of the pion have previously been constrained in the $x \gtrsim 0.1$ region using Drell–Yan data and direct photon production data obtained by πp scattering experiments (see for example [53–57]). Our determination using $F_2^{\text{LN}(3)}$ is the first result which constrains the pion structure function at values of x which are more than an order of magnitude smaller. Background contributions and possible absorptive corrections [9, 46, 47], which have not been taken into account, are expected to only affect the absolute normalization of our result since all of the data are at $z = 0.7$.

7 Summary and conclusions

The semi-inclusive cross sections $ep \rightarrow epX$ and $ep \rightarrow enX$ have been measured in the kinematic region $2 \leq Q^2 \leq 50 \text{ GeV}^2$, $6 \times 10^{-5} \leq x \leq 6 \times 10^{-3}$ and $p_T \leq 200 \text{ MeV}$. Comparison of the proton and neutron data in the same kinematic domain shows that the production cross section for leading protons is larger than it is for leading neutrons. This result demonstrates that leading proton production cannot be entirely due to pion exchange.

The LEPTO Monte Carlo program, which is based upon soft colour interactions and a string fragmentation model, describes the magnitude and the general shape of the neutron data with $z \geq 0.3$. It fails, however, to describe the rate of leading proton production and the rise

in the semi-inclusive structure function $F_2^{\text{LP}(3)}$ as a function of Q^2 . The RAPGAP Monte Carlo program, which simulates pion exchange, gives an acceptable description of the neutron data with $z \geq 0.7$ but does not explain the absolute rate of leading proton production.

The proton and neutron data are equally well described by fits assuming factorization in x, Q^2 and z or β, Q^2 and z . The scaling violations observed in the measured semi-inclusive structure functions $F_2^{\text{LP}(3)}$ and $F_2^{\text{LN}(3)}$ are similar in size and shape and are close to those seen in the GRV parametrizations of the inclusive structure functions of the pion and the proton.

The neutron and proton data are reasonably well described by a Regge model of leading baryon production which considers the colour neutral exchanges of pions, pomerons and secondary reggeons. The semi-inclusive cross sections for leading neutrons with $0.7 \leq z \leq 0.9$ can be described entirely by π^+ exchange whereas the semi-inclusive cross sections for protons with $0.73 < z < 0.88$ require π^0 and f_2 exchange contributions. In our model, the contribution due to f_2 exchange is approximately a factor of two greater than the contribution due to π^0 exchange. The β and Q^2 dependence of the leading neutron data at $z = 0.7$ are consistent with the GRV leading order parton distributions for the pion.

Acknowledgements. We are grateful to the HERA machine group whose outstanding efforts have made and continue to make this experiment possible. We thank the engineers and technicians for their work in constructing and now maintaining the H1 detector, our funding agencies for financial support, the DESY technical staff for continual assistance, and the DESY directorate for the hospitality which they extend to the non-DESY members of the collaboration. The forward proton spectrometer was supported by the INTAS93-43 project.

References

1. ZEUS Collaboration, M. Derrick, et al., Phys. Lett. B **315**, 481 (1993)
2. H1 Collaboration, T. Ahmed, et al., Nucl. Phys. B **429**, 477 (1994)
3. H1 Collaboration, T. Ahmed, et al., Phys. Lett. B **348**, 681 (1995)
4. ZEUS Collaboration, M. Derrick, et al., Z. Phys. C **68**, 569 (1995)
5. H1 Collaboration, C. Adloff, et al., Z. Phys. C **76**, 613 (1997)
6. ZEUS Collaboration, J. Breitweg, et al., Eur. Phys. J. C **2**, 237 (1998)
7. J.D. Sullivan, Phys. Rev. D **5**, 1732 (1972)
8. H. Holtmann, et al., Phys. Lett. B **338**, 363 (1994)
9. B. Kopeliovich, B. Povh, I. Potashnikova, Z. Phys. C **73**, 125 (1996)
10. A. Szczurek, N.N. Nikolaev, J. Speth, Phys. Lett. B **428**, 383 (1998)
11. G. Ingelman, A. Edin, J. Rathsman, Comp. Phys. Commun. **101**, 108 (1997)
12. W. Buchmüller, A. Hebecker, Phys. Lett. B **355**, 573 (1995)

13. A. Edin, G. Ingelman, J. Rathsman, Phys. Lett. B **366**, 371 (1996)
14. T. Sjöstrand, Comp. Phys. Commun. **82**, 74 (1994)
15. L. Trentadue, G. Veneziano, Phys. Lett. B **323**, 201 (1994)
16. D. de Florian, R. Sassot, Phys. Rev. D **58**, 54003 (1998)
17. M. Grazzini, L. Trentadue, G. Veneziano, Nucl. Phys. B **519**, 394 (1998)
18. H1 Collaboration, I. Abt, et al., Nucl. Instrum. Meth. A **386**, 310 (1997); *ibid.* 348
19. H1 SPACAL Group, T. Nicholls, et al., Nucl. Instrum. Meth. A **374**, 149 (1996)
20. H1 SPACAL Group, R.-D. Appuhn, et al., Nucl. Instrum. Meth. A **386**, 397 (1997)
21. H1 Calorimeter Group, B. Andrieu, et al., Nucl. Instrum. Meth. A **336**, 499 (1993)
22. H1 Collaboration, *The Forward Proton Spectrometer of H1*, Contributed paper pa17-025 to the 28th International Conference on High Energy Physics ICHEP'96, Warsaw, Poland, July 1997
23. B. List, Ph.D. Thesis, University of Hamburg, 1997
24. D. Acosta, et al., Nucl. Instrum. Meth. A **294**, 193 (1990)
25. WA89 Collaboration, A. Forino, et al., Proposal CERN/SPSC-87/43, 1987
26. M. Beck, et al., Nucl. Instrum. Meth. A **381**, 330 (1996)
27. Application Software Group, *GEANT Detector Description and Simulation Tool*, CERN Program Library Long W5013, October 1994
28. T. Nunnemann, Diploma Thesis, University of Heidelberg, 1996
29. T. Nunnemann, Ph.D. Thesis, University of Heidelberg (in preparation)
30. W. Flauger, F. Mönnig, Nucl. Phys. B **109**, 347 (1976)
31. V. Blobel, et al., Nucl. Phys. B **135**, 379 (1978)
32. H. Holtmann, et al., Nucl. Phys. A **596**, 631 (1996)
33. C. Scheel, Ph.D. Thesis, University of Amsterdam, 1994
34. U. Bassler, G. Bernardi, Nucl. Instrum. Meth. A **361**, 197 (1995)
35. H. Jung, Comp. Phys. Commun. **86**, 147 (1995)
36. L. Lönnblad, Comp. Phys. Commun. **71**, 15 (1992)
37. V. Blobel, *Unfolding Methods in High-Energy Physics Experiments*, DESY Report, 84-118 (1984); *Proceedings from the 1984 CERN School of Computing*, Aiguablava, Spain, CERN 85-02
38. A. Kwiatkowski, H. Spiesberger, H.-J. Möhring, Comp. Phys. Commun. **69**, 155 (1992)
39. M. Glück, E. Reya, A. Vogt, Z. Phys. C **67**, 433 (1995); Z. Phys. C **53**, 651 (1992)
40. H. Plochow-Besch, Comp. Phys. Commun. **75**, 396 (1993)
41. J. Benecke, et al., Phys. Rev. **188**, 2159 (1969); T.T. Chou, C.N. Yang, Phys. Rev. D **50**, 590 (1994)
42. H1 Collaboration, S. Aid, et al., Nucl. Phys. B **470**, 3 (1996)
43. K. Golec-Biernat, J. Kwieciński, A. Szczurek, Phys. Rev. D **56**, 3955 (1997)
44. Yu.M. Kazarinov, et al., Sov. Phys.-JETP **43**, 598 (1976)
45. R.G.E. Timmermanns, Th.A. Rijken, J.J. de Swart, Phys. Rev. Lett. **67**, 1074 (1991)
46. N.N. Nikolaev, J. Speth, B.G. Zakharov, *Absorptive Corrections to the One Pion Exchange and Measurability of the Small- x Pion Structure Function at HERA*, KFA-IKP-TH-97-17, 1997, hep-ph/9708290
47. U. D'Alesio, H.J. Pirner, A. Schäfer, *Target Fragmentation in pp and γp Collisions at High-Energies*, HD-TVP-98-3, hep-ph/9806321
48. Yu.L. Dokshitzer, Sov. Phys.-JETP **46**, 641 (1977); V.N. Gribov, L.N. Lipatov, Sov. J. Nucl. Phys. **15**, 438 (1972); G. Altarelli, G. Parisi, Nucl. Phys. B **126**, 298 (1977)
49. ZEUS Collaboration, J. Breitweg, et al., Eur. Phys. J. C **1**, 81 (1998)
50. J.F. Owens, Phys. Rev. D **30**, 943 (1984)
51. P. Aurenche, et al., Phys. Lett. B **233**, 517 (1989)
52. P.J. Sutton, et al., Phys. Rev. D **45**, 2349 (1992)
53. J.S. Conway, et al., Phys. Rev. D **39**, 92 (1989)
54. J. Badier, et al., Z. Phys. C **18**, 281 (1983)
55. B. Betev, et al., Z. Phys. C **28**, 9 (1985)
56. M. Bonesini, et al., Z. Phys. C **37**, 535 (1988)
57. C. de Marzo, et al., Phys. Rev. D **36**, 8 (1987)